International Journal of Material Forming (2021) 14:961–972
https://doi.org/10.1007/s12289-021-01612-0

ORIGINAL RESEARCH

Mold filling simulation and experimental investigation of metallic feedstock used in low-pressure powder injection molding

Mohamed Azzouni [1] · Vincent Demers [1] · Louis Dufresne [1]

Received: 28 July 2020 / Accepted: 6 January 2021 / Published online: 18 January 2021
© The Author(s), under exclusive licence to Springer-Verlag France SAS part of Springer Nature 2021

Abstract

The mold filling stage of the low-pressure powder injection molding process was simulated numerically and validated by experimental injections. For this, a feedstock formulated from a 17-4PH stainless steel powder (60 vol.%) and a wax-based binder system (40 vol.%) was used. The feedstock was characterized to obtain its thermal properties and rheological profiles at different temperatures. These were then implemented into the Autodesk Moldflow Synergy 2019 package, the numerical tool used for the simulation. The numerical results, including those pertaining to the injected length, the melt front velocity, and the pressure, were validated using a laboratory experiment set-up made of an injection press and two instrumented molds. The injected lengths predicted by the simulation were similar to the experimental short-shot results, with a relative difference below 0.5%. Since the injections were performed at constant volumetric flow, the injected length was not influenced by the feedstock temperature, but only by the shape of the mold cavity. Numerical and experimental results for the pressure were also compared. The agreement between the was good except at the end of the injection process. It is conjectured that the disagreement observed might be due to a difference in boundary conditions. The physical mold not being "air-tight" as the numerical one, an excess pressure could have been present in the latter. As a final note, this interesting simulation capability to predict the injection pressure experienced by a low-pressure (metallic or ceramic) powder injection molding feedstock was, to the best of the authors' knowledge, for the first time, validated experimentally in this study using a low-pressure sensor placed in the mold during real-scale LPIM injections.

Keywords Low-pressure powder injection molding · Numerical simulation · Metallic powder · Feedstock · Mold filling

Introduction

Powder injection molding (PIM) is a shaping technique used to produce small and complex shape parts from metallic powders. This manufacturing technology consists in combining a powder with a polymer binder to form a feedstock that is injected into a mold cavity. After molding, the resulting green part is then debound and sintered to extract the binder and obtain a metallic component exhibiting density close to the theoretical one [1]. Depending on the feedstock viscosity, the PIM technology can be categorized under two approaches, namely high-pressure powder injection molding (HPIM) and low-pressure powder injection molding (LPIM). The first approach uses high-viscosity feedstocks ranging from 100 to 1000 Pa·s, which are injected into mold cavities using a high pressure typically varying from 20 to 200 MPa [2]. The second approach uses low-viscosity feedstocks (< 100 Pa·s) that are injected at pressures generally lower than 1 MPa (typically varying from 10 to 500 kPa [3, 4]). Although the manufacturing readiness level of the LPIM approach is significantly lower than the HPIM approach, the LPIM process has demonstrated important benefits. It can become cost-effective, either in low- or in high-production volumes, due to the reduction in the size of the injection machines and of the mold shells, which occurs thanks to a significant reduction in injection pressures [5]. Initially used in ceramics shaping [6–9], the LPIM technology has quickly become attractive for the

✉ Vincent Demers
vincent.demers@etsmtl.ca

Mohamed Azzouni
mohamed.azzouni.1@ens.etsmtl.ca

Louis Dufresne
Louis.dufresne@etsmtl.ca

[1] École de technologie supérieure, 1100 Notre-Dame West, Montreal, QC H3C 1K3, Canada

development of high value-added metallic parts in the aerospace and medical industries. As a pioneer in the development of LPIM process, Goncalves [10] proved that this shaping approach could be used successfully for metallic-based feedstocks. Few years later, Julien et al. [11] demonstrated that PIM technology could be used at low-pressure to produce gas turbine engine parts made from superalloys. Using high added value material, Nor et al. [12] proposed a novel binder system containing palm stearin to formulate titanium-based feedstocks exhibiting low viscosity. Aslam et al. [13] demonstrated that metallic-based feedstocks can be formulated at high solid loading while keeping a low viscosity required for LPIM process. However, Fareh et al. [14] highlighted that such kind of low-viscosity feedstocks exhibit a propensity to segregation that may occur either during rheological testing or during injection stage. Recently, Zhang et al. [15] demonstrated that sacrificial molds could be used in LPIM process due of the very low pressure (i.e., < 2 MPa in this study) required at the injection stage.

Mold filling is one of the most important steps of the PIM process that must be controlled in order to obtain a complete mold filling while avoiding defects such as voids, sinks, jetting, welding lines, warpage, and cracks. Numerical simulations have been successfully used to predict different physical quantities, such as the material flow behavior, filling times, the melt front velocity, and the pressure in the mold cavity, in order to optimize the process parameters and overcome molding defects [16]. For metallic-based feedstocks, the injection stage has mostly been simulated for high-viscosity powder-binder mixtures generally developed for the HPIM process. Ilinca et al. [17] used Plasview3D to investigate the pattern of the flow injected into an "M" shape cavity, which was validated using short-shot injections, thus confirming the non-uniform flow in the cavity predicted by this package. The same research team used stainless steel-based feedstock to assess the injection pressure within a rectangular part, where the experimental pressure recorded from two different positions confirmed the simulation results obtained by Plasview3D [18]. Ahn et al. [19] proposed to combine filling and cooling analyses to improve the accuracy of numerical simulations during the mold filling of a stainless steel-based feedstock. They found that the accuracy of the pressure values predicted by the PIMsolver package increases when a slip (boundary condition) behavior is introduced into the model. Tseng et al. [20] used Moldex3D to investigate the powder segregation phenomenon occurring during the injection stage. The numerical results obtained with a suspension balance model provided by the software predicted segregation lines in the vicinity of the gate that were also experimentally validated using nuclear magnetic resonance imaging. Zheng et al. [21] implemented a second-order rheological model in MoldFlow to confirm that the predicted pressure profiles were in good agreement with the experimental results, and finally used the numerical simulations to redesign the gate and optimize the injection process parameters. Bilovol et al. [22, 23] confirmed that the rheological model used by simulation software is one of the most important parameters for the numerical simulation of the injection stage. Using a stainless steel-based feedstock used in HPIM processes, they also compared the pressures and temperatures simulated by Moldflow, C-Mold, and ProCAST with experimental results before concluding that the Moldflow software was the most promising commercial package for predicting flow patterns, weld line locations, and temperature profiles.

For LPIM processes, the numerical simulation of the injection stage has received, to the best of the authors' knowledge, only limited attention in a few recent studies. Sardarian et al. [24, 25] used Moldflow Synergy to predict the filling time and pressure for an alumina-based feedstock used in LPIM. The same research team also showed the powerful capacity of the Moldflow Synergy package to understand better the influence of temperature, pressure, and flow rate on the jetting phenomenon, and to optimize injection parameters [26]. Ben Trad et al. [27] confirmed the ability of the Moldflow package to simulate successfully the injected length, the melt front velocity, the filling time, and the segregation phenomenon for a metallic-based feedstock in LPIM [28]. Although the potential to predict the flow behavior of metallic- or ceramic-based LPIM feedstocks has been demonstrated, the simulated injection pressures obtained by these previous research teams have never been validated with experimental measurements. The aim of this study is to verify the ability of the Moldflow simulation tool to predict the in-cavity pressure during the injection stage of LPIM metallic feedstock.

Numerical model

The Moldflow model is defined by the following governing equations, which describe the conservation of mass, momentum, and energy, as well as the material behavior and boundary conditions.

Conservation of mass:

$$\frac{\partial \rho}{\partial t} + \nabla \cdot (\rho u) = 0 \tag{1}$$

Conservation of momentum:

$$\rho \frac{\boldsymbol{Du}}{Dt} = -\nabla \rho + \nabla \cdot \boldsymbol{\tau} + \rho \mathbf{g} \tag{2}$$

Conservation of energy:

$$\rho C_\rho \frac{DT}{Dt} = \nabla \cdot (k \nabla T) + \boldsymbol{\tau} : \nabla \boldsymbol{u} + \beta T \frac{Dp}{Dt} \tag{3}$$

where the material derivative is defined by:

$$\frac{D(\cdot)}{Dt} = \frac{\partial(\cdot)}{\partial t} + \boldsymbol{u}\cdot\nabla(\cdot) \tag{4}$$

and p is the pressure, t is the time, ρ is the density, $\boldsymbol{u}$ is the velocity vector, $\boldsymbol{g}$ is the gravitational acceleration, T is the temperature, C_p is the specific heat, k is the thermal conductivity, $\boldsymbol{\tau}$ is the viscous stress tensor, and β is the polymer expansivity, which is defined as follows:

$$\beta = -\frac{1}{\rho}\frac{\partial \rho}{\partial T} \tag{5}$$

In Moldflow, the evolution of viscosity according to the shear rate and temperature is described using either Cross-WLF or second-order models. The choice of one or the other of these models depends on the shape of the viscosity profile [29, 30]. The Cross-WLF model described in Eqs. (6) and (7) is used when the viscosity remains constant at low shear rates and shows an important and continuous decrease over the high shear rate range.

$$\eta = \frac{\eta_0}{1 + \left(\frac{\eta_0 \dot{\gamma}}{\tau^*}\right)^{1-n}} \tag{6}$$

whereη_0 is the zero shear viscosity described by:

$$\eta_0 = C \exp\left(-\frac{A \cdot (T-D)}{B + (T-D)}\right) \tag{7}$$

and where η is the viscosity of molten feedstock, $\dot{\gamma}$ is the shear deformation rate, T is the absolute temperature, and all parameters, namely, n, the power law index, τ^* the critical shear stress at the transition to shear thinning, and A, B, C, and D, are data-fitted coefficients. The second-order model described in Eq. (8) is used when the viscosity quickly decreases at low shear deformation rates and shows a Newtonian plateau at high shear rates [31, 32]:

$$\begin{aligned} 1\mathrm{n}(\eta) = {} & E + F\ 1n\left(\dot{\gamma}\right) + GT + H\left[1n\left(\dot{\gamma}\right)\right]^2 \\ & + I\ 1n\left(\dot{\gamma}\right)T + JT^2 \end{aligned} \tag{8}$$

where η, $\dot{\gamma}$, and T were defined above, and E to J are the data-fitted coefficients. The process parameters used for the numerical simulations, as well as for the real-scale injections, are reported in Table 1. Generally heated between 30 and 50 °C and based on preliminary injection tests, the mold temperature was set at 40 °C to enhance feedstock moldability but prevent sticking of the injected parts during ejection stage. The minimum feedstock temperature was set at 80 °C just slightly higher than its melting point (i.e., 77.5 °C), while maximum feedstock temperature was limited to 100 °C to avoid evaporation and/or chemical degradation of such kind of wax-based binders. The piston speeds and the related volume flow rate represent the maximum injection rate of the electric piston installed on the laboratory injection press.

Table 1 Process parameters used for the numerical simulations and real-scale injections

Mold temperature (°C)	40
Feedstock temperature (°C)	80, 90, and 100
Piston speed (mm/s)	11.8
Volume flow rate (cm^3/s)	2.3

Model input and validation data

Feedstock preparation

Water-atomized stainless steel 17-4PH powder (Epson Atmix Corporation, Japan) was combined with a wax-based binder at 60 vol.% of powder to formulate the feedstock. A scanning electron microscope (Hitachi 3600, secondary electrons detector) was used to assess the particle shape of the dry powder (Fig. 1a), while the particle size characterized by D_{10}, D_{50}, and D_{90} at 3.4, 11.8, and 31.3 μm, respectively, was measured using an LS 13320 Beckman Coulter laser diffraction particle analyzer (Fig. 1b). The binder system was formulated from paraffin wax, carnauba wax, stearic acid, and ethylene vinyl acetate according to the proportions given in Table 2. These constituents were selected due to their extensive use in LPIM. They facilitate the ejection of the part after the filling stage, and to promote the surfactant and thickening effects. Furthermore, they enhance the chemical links between the powder and binder while controlling the segregation phenomena [33–35].

The melting points and density of each single binder constituent are given in Table 2. According to the ASTM B923–16 standard method [36], an AccuPyc II 1340 helium gas pycnometer was used to determine the density of the metallic powder, binders, and feedstock, while the melting point of each binder and feedstock was evaluated using a Perkin Elmer Pyris 1 DSC according to the ASTM D3418–15 standard [37]. The DSC tests were performed over temperatures ranging from 20 to 120 °C, using a heating rate of 10 °C/min, under a dry nitrogen gas flow rate of 50 mL/min. The feedstock melting point of 77.5 °C was determined from the last peak obtained during the second heating cycle.

Feedstock characterization

To ensure accurate flow simulations, the feedstock properties were characterized using melt rheology, calorimetry,

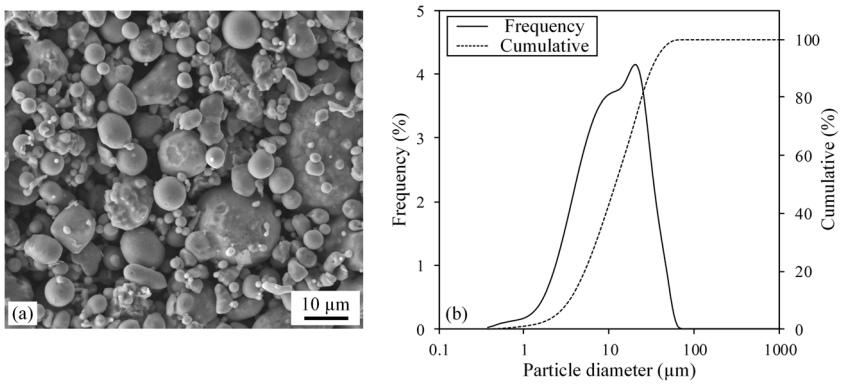

Fig. 1 (a) SEM micrograph and (b) particle size distribution of 17-4PH dry powder

and thermal conductivity. The feedstock viscosity profiles reported in Fig. 2a were measured using an Anton Paar MCR 302 rotational rheometer with a measuring cylinder and cup configuration (CC-17) placed into the temperature-controlled measuring system C-PTD 200. At three different temperatures (80, 90, and 100 °C) a molten feedstock was poured into the cup of the rheometer, and then a shear rate ranging from 0.5 to 3500 s^{-1} was applied. The experimental viscosity profiles were obtained by repeating each condition three times to calculate average viscosity profiles for each condition. The experimental profiles were fitted according to the rheological model presented in Eqs. (6) to (8) using Matlab to obtain the fitting coefficients reported in Table 3, which were finally implemented into Moldflow. In this project, the quasi-Newtonian plateaus observed for all testing temperatures in Fig. 2a were captured best by the second-order model given in Eq. (8).

The specific heat (C_p) of the feedstock was obtained with a PerkinElmer Pyris 1 differential scanning calorimeter (DSC) according to ASTM-E1269 [38], using the same procedure described above for the melting point, and reported in Fig. 2b. The feedstock thermal conductivity (k) presented in Fig. 2c was obtained at different temperatures using a Quantum Design Physical Property Measurement System (PPMS P670) with a Thermal Transport Option (TTO) according to the test method given in [39]. These thermal properties (i.e., C_p and k) were implemented in Moldflow as a material law matrix.

Numerical and experimental mold geometries and set up

Numerical simulations of the injection stage were performed in two different mold cavities using Moldflow Synergy 2019 (Autodesk Inc.). The rectangular and hourglass 3D models illustrated in Fig. 3a-b were meshed using 3D tetrahedral elements containing between 1 and 4 million elements according to the thickness of the part, which was varied from 3 to 5 mm. The morphology and the mesh size of 0.5 mm illustrated in Fig. 3c-d offer a good compromise between the accuracy of the results and an adequate time required for simulations. Indeed, the mesh sensitivity analysis reported in Fig. 3e confirms that below 0.5 mm, the injection pressure results become independent of the mesh size, but that the simulation time is significantly affected.

Simulation results (injected length, melt front velocity, and pressure) were then validated using a laboratory injection press and the two instrumented molds illustrated in Fig. 4 that were equipped with piezo-resistive pressure sensors (series 25Y, Omni instruments: maximum pressure of 50 kPa and accuracy ± 0.25 kPa). The flow pattern and the melt front velocity were experimentally measured using the methodology developed by Pengcheng et al. [40], where the steel upper-plate illustrated in Fig. 4 was replaced by a transparent material. In this study, the injections were recorded using a camera (30 frames per second) and post-processed using the Avimeca and Regressi software packages to obtain the melt front position and velocity.

Table 2 Melting point, density, and proportion of feedstock constituents

Constituents	Melting point (°C)	Density (g/cm^3)	Volume fraction (vol.%)
17–4 PH powder	> 1404	7.69	60
Paraffin wax (PW)	58.8	0.91	30
Carnauba (CW)	84.5	1.00	7
Stearic acid (SA)	73.9	1.00	2
Ethylene vinyl acetate (EVA)	49.0	0.98	1

Table 3 Fitting coefficients of the second-order and Cross-WLF viscosity models

Fitted Coefficient	Value
n	4.464 E-1
τ^* *(Pa)*	4.693 E-2
A	1.290 E1
B (K)	6.118 E1
C (Pa·s)	9.937 E6
D (K)	2.767 E2
E	5.794
F	−7.673 E-1
G	−5.995 E-2
H	5.843 E-2
I	−1.258 E-3
J	2.522 E-4

Results and discussion

Injected length and filling time

A qualitative comparison between the simulated and experimental short-shot results is shown in Fig. 5a-c for three different filling stages. The injected lengths obtained at different temperatures for the rectangular mold cavity are reported in Fig. 5d. Since the injections were performed at constant volumetric flow, the injected length was not influenced by the feedstock temperature. In this injection approach, a constant stroke plunger controls the injection flow, and thus, the injected length instead of the feedstock properties. A non-constant pressure profile is expected to be developed inside the mold cavity (this topic is investigated below). In other words, the injected length depends on the shape of the mold cavity, instead of on the feedstock properties when this injection principle is used. Similarly to the results obtained by Ben Trad et al. [27], the injected lengths obtained experimentally and numerically were in a good agreement, with a relative difference less than 0.5%.

The evolution of the melt front velocity along the flow direction according to the injected length is presented in Fig. 6a-b for both mold cavities (rectangular and hourglass) and different injection temperatures (80, 90, and 100 °C). As expected, the velocity profile is completely different for the two mold geometries. During gate filling, a transitory zone is characterized by an acceleration, for the rectangular shape (Fig. 6a), and a rather constant feedstock velocity, for the hourglass shape (Fig. 6b). During the first seconds of the mold filling, this transitional regime illustrated by vertical phantom lines in Fig. 6a-b corresponds to the expansion of the feedstock passing from a non-constrained to a constrained fluid, as illustrated in Fig. 6c-d. Since the injected length was measured from the zero position indicated in Fig. 6c-d, the feedstock velocity obtained in a constant rectangular cross-section mold cavity remains almost constant at around 2 cm/s when the gate is completely filled. During the hourglass part filling, the melt flow velocity follows a concave down profile instead, due to the continuous decrease in the cross-section mold cavity,

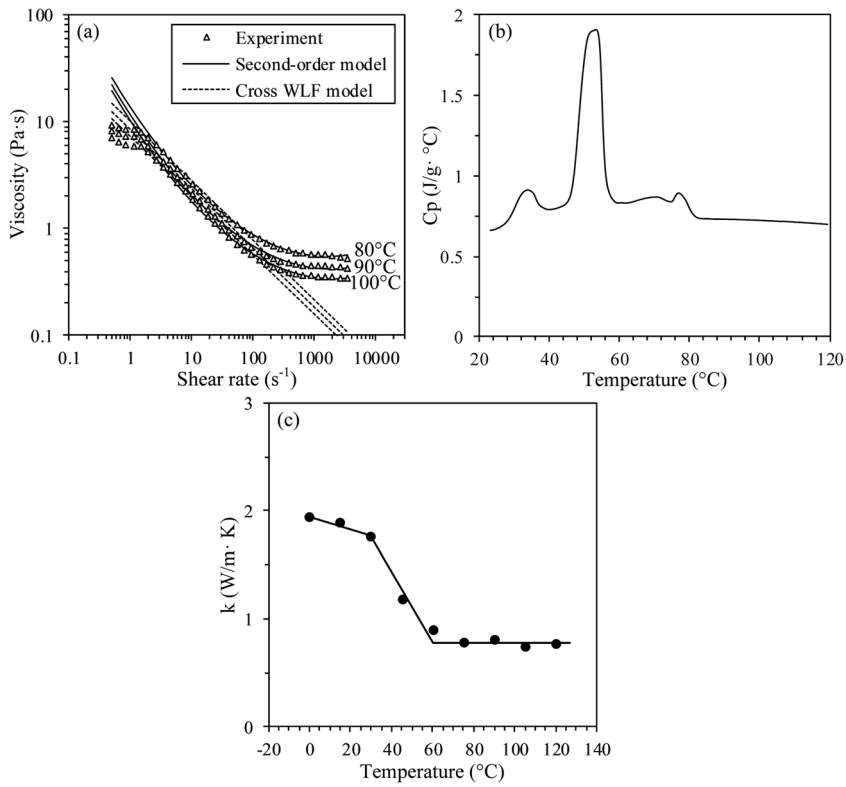

Fig. 2 Rheological and thermal properties of feedstock: (a) viscosity profiles with superimposed second-order and Cross-WLF models, (b) specific heat, and (c) thermal conductivity measured at different temperatures

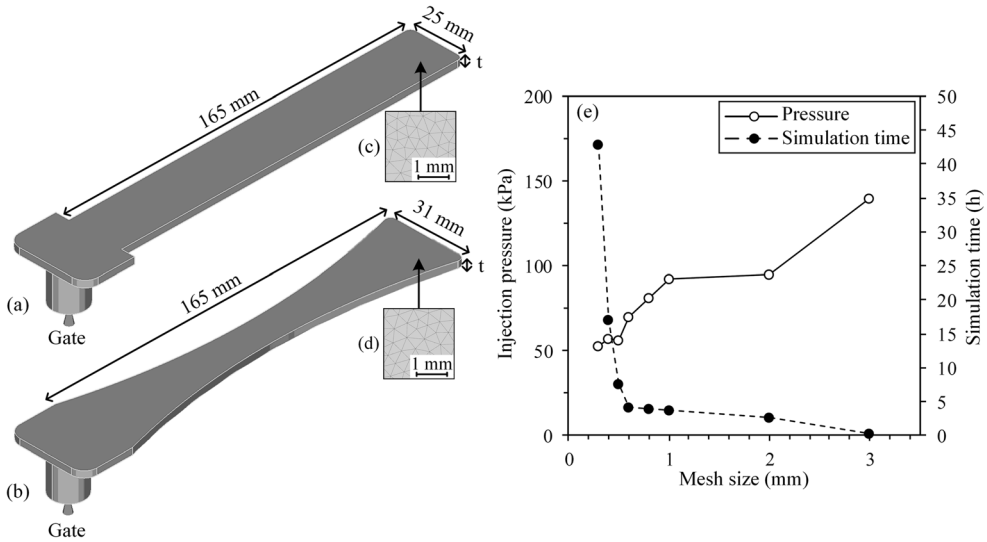

Fig. 3 (a-b) 3D view of the rectangular and hourglass mold cavities with (c-d) the superimposed tetrahedral finite element mesh, (e) evolution of the pressure at the gate and the simulation time according to the mesh size.

where the feedstock velocity reaches its maximum value of 3.1 cm/s in the center of the part. Downstream from this maximum velocity value, and as observed by Bosioc et al. [41], the melt front decreases due to the increase in the cross-section mold cavity. For the two mold geometries, the simulated melt front velocities were in a good agreement with the experimental observations, irrespective of the feedstock temperature, with a maximum relative difference of 3.7% (a difference of 8.6% was found during the gate filling).

Influence of temperature on injection pressure

The pressure profiles developed in the mold cavity during typical injections at 80 °C are presented in Fig. 7a-b, where the notations P1 to P4 in Fig. 7a and P1 to P3 in Fig. 7b refer to the sensor position illustrated in Fig. 4a-b. In general, the measured pressure profiles can be divided into three zones. During the gate filling, the pressure remains at zero because no feedstock is in contact with the sensor. Note that this value remains at zero over a longer filling stage as the sensor is positioned far from the gate. Just before the feedstock/sensor contact, a negative pressure value was systematically measured experimentally for all sensor positions, cavities, and feedstock temperatures. This minor, but unexpected, reading was attributed to a sensor preheating-phenomenon produced by an increase in air temperature downstream from the feedstock melt front. These temporal decreases in pressure were not modeled, and were thus not seen in the

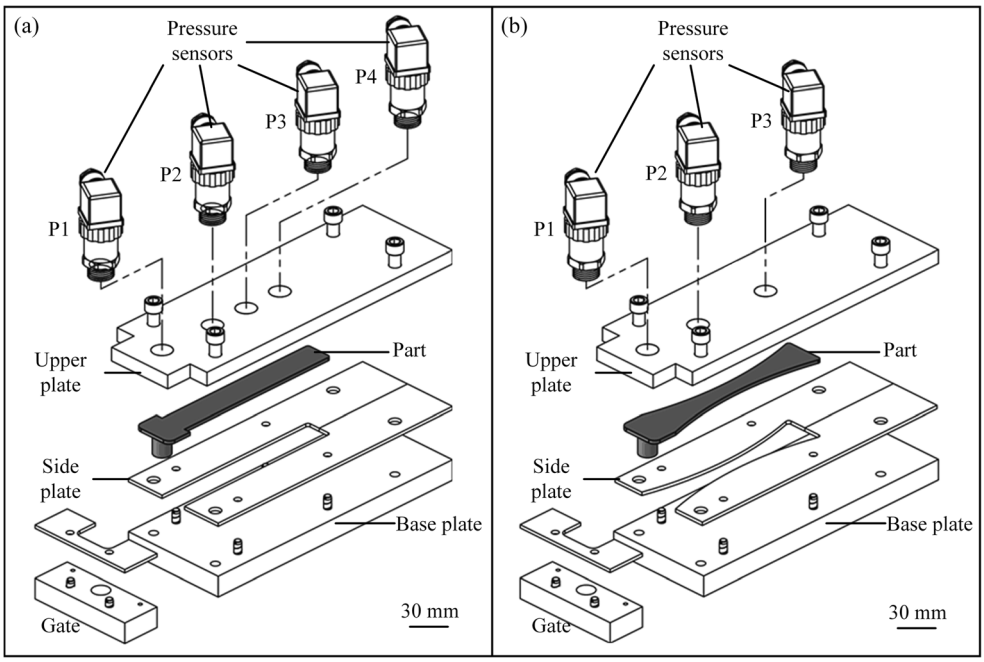

Fig. 4 Exploded view of the (a) rectangular, and (b) hourglass mold cavities showing the location of the pressure sensors

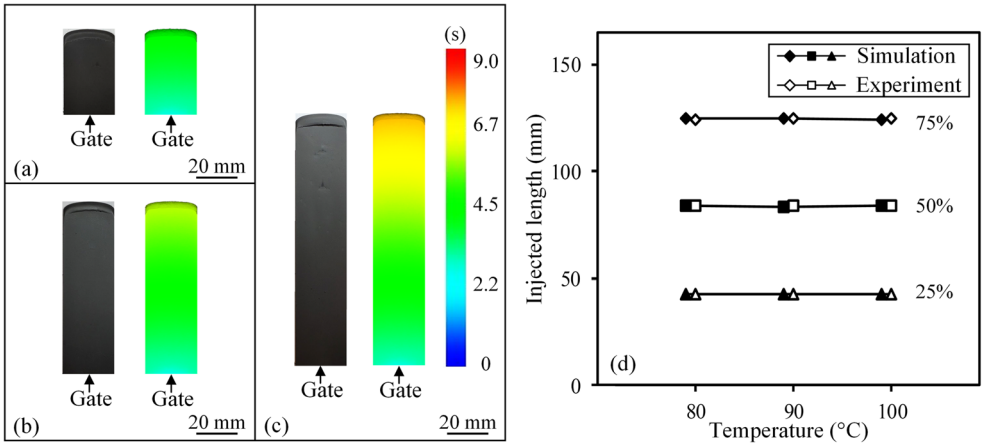

Fig. 5 Experimental and simulated injected lengths: (a-c) typical short shots obtained at 25, 50, and 75% filling stages, with feedstock at 90 °C injected in the rectangular mold, and (d) injected lengths for different injection temperatures, and filling stages (the marks are horizontally shifted for better clarity)

numerical simulations. As the melt front reaches the sensor surface (e.g., for the filling stage higher than 5% located at the sensor P1 in Fig. 7a), the pressure starts to increase, up to where the mold is completely filled. During this filling stage, the local pressure continuously increases to overcome the internal friction experienced by the molten feedstock. In general, the simulated pressure profiles obtained in Fig. 7a-b are in good agreement with experiments over the majority of the mold filling range, but diverge during the last part of the mold filling.

The injection pressures obtained numerically and experimentally at positions P1 were extracted at different filling stages for different injection temperatures, and are reported in Fig. 7c-d for both cavities. As can be qualitatively seen in the pressure profiles, the simulated pressures at different injection temperatures are similar to those obtained experimentally, with a maximum relative difference of about 8.3%, except at the end of the mold filling, where this value reaches 33.1%. This overestimation of the simulated pressure occurring only over the last moment of the filling stage could be

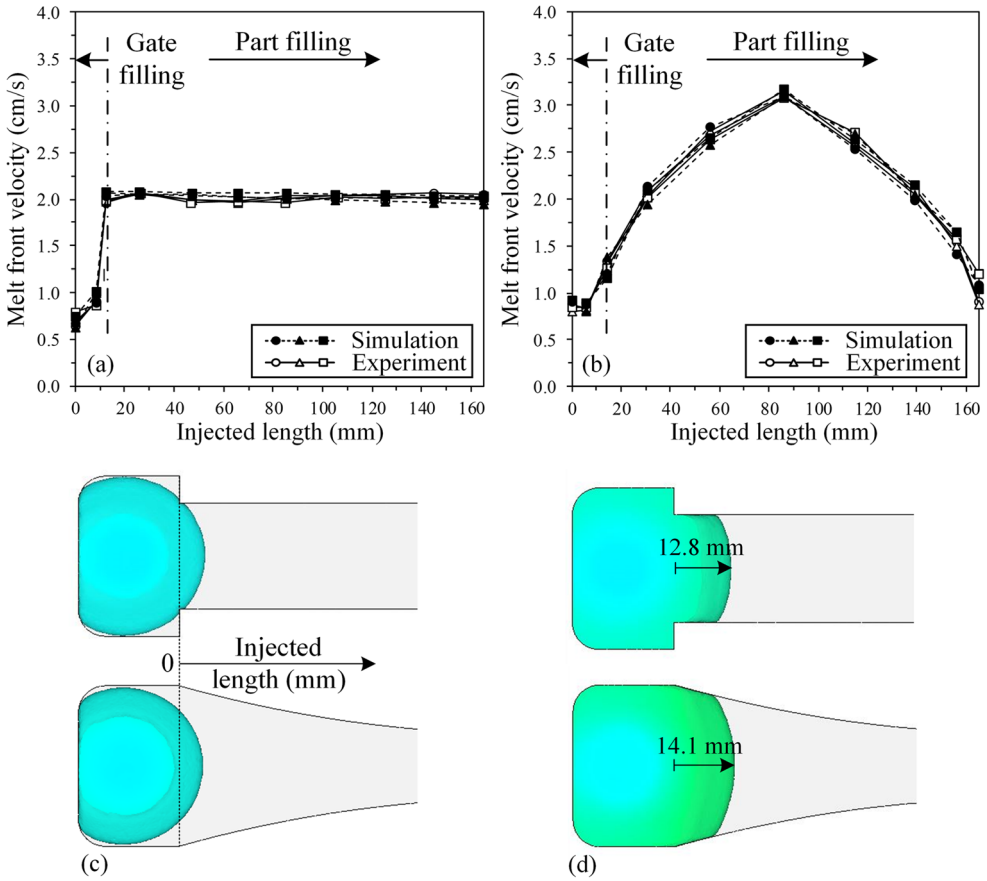

Fig. 6 Simulated and experimental melt front velocity of: (a) the rectangular part and (b) hourglass parts for different injection temperatures (with circles, triangles, and squares representing tests performed at 80, 90, and 100 °C, respectively), and top view of the mold cavities showing the melt front (c) during the gate filling, and (d) after the gate is completely filled, illustrating how the injected length was measured

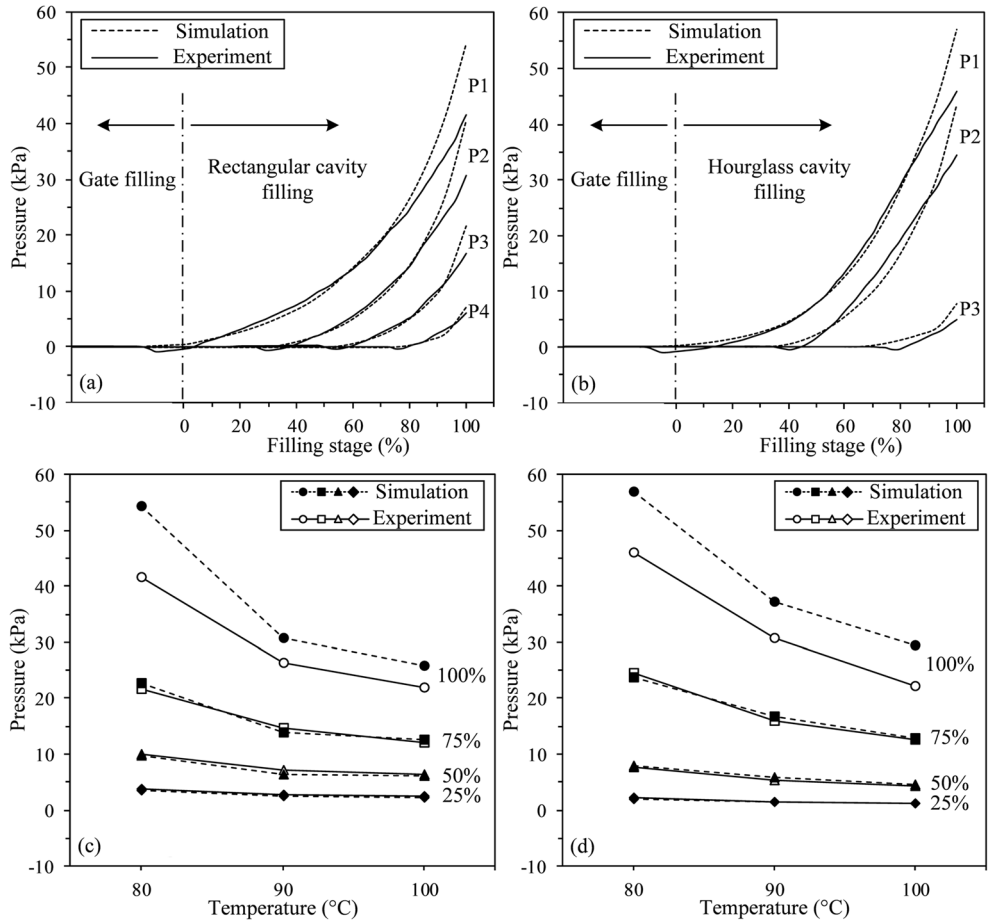

Fig. 7 (a-b) Typical simulated and experimental pressure profiles obtained at different sensor positions for both cavities at 80 °C, (c-d) comparison of experimental and simulated pressures at different filling stages (in %) and injection temperatures (measured at position P1 using a mold thickness of 4 mm).

explained by a boundary condition/end effect. In fact, mold cavities are not air-tight and so there is no actual pressure build-up inside the mold. The difference in pressure observed at the end of the mold filling, together with the design of a more physically appropriate boundary condition, will be studied in a future work. For injections performed at constant volumetric flow, the decrease in injection pressure with an increase in the melt temperature seen in Fig. 7c-d for both cavities was expected, due to the intrinsic decrease in feedstock viscosity illustrated in Fig. 2a.

Influence of thickness on the injection pressure

The influence of mold thickness on the injection pressure is presented in Fig. 8 for the rectangular and hourglass mold geometries at the sensor position P1, using a constant injection temperature (90 °C). As seen in the previous section, the three distinct zones are visible in Fig. 8a-b for both mold geometries, even when using another mold thickness (i.e., zero, negative, and increase in pressure). The injection pressures obtained numerically and experimentally at position P1 were extracted from such pressure profiles at different filling stages, for three different thicknesses of 3, 4, and 5 mm, and are reported in Fig. 8c-d for both cavities. As expected, an increase in mold thickness produces a decrease in injection pressure, since an increase in overall cross-section mold cavity requires less pressure to inject the same constant flow, or in other words, to inject the same feedstock flow, using the same injection force applied by the piston. For the different mold thicknesses used, the pressures obtained by numerical simulation were in very good agreement with the experimental measurements. This was observed for the majority of the mold filling time. More specifically, a difference of less that 7.6% was observed. In fact, the agreement was excellent for about 75% of the filling process. It only at the end of the filling that a divergence in values was observed (a numerical overpressure). It is conjectured that this perhaps may be due to a difference in boundary conditions. Indeed the experimental mold was not air tight as opposed to the numerical boundary condition, which did not allow the imprisoned air to escape from the mold. Note finally that this overpressure obtained at the end of the simulated injection was visible regardless of the mold thickness.

Prediction of the pressure at the end of the mold filling using a phenomenological model

Because predicting the pressure along the whole injection stage is essential, a phenomenological model was proposed

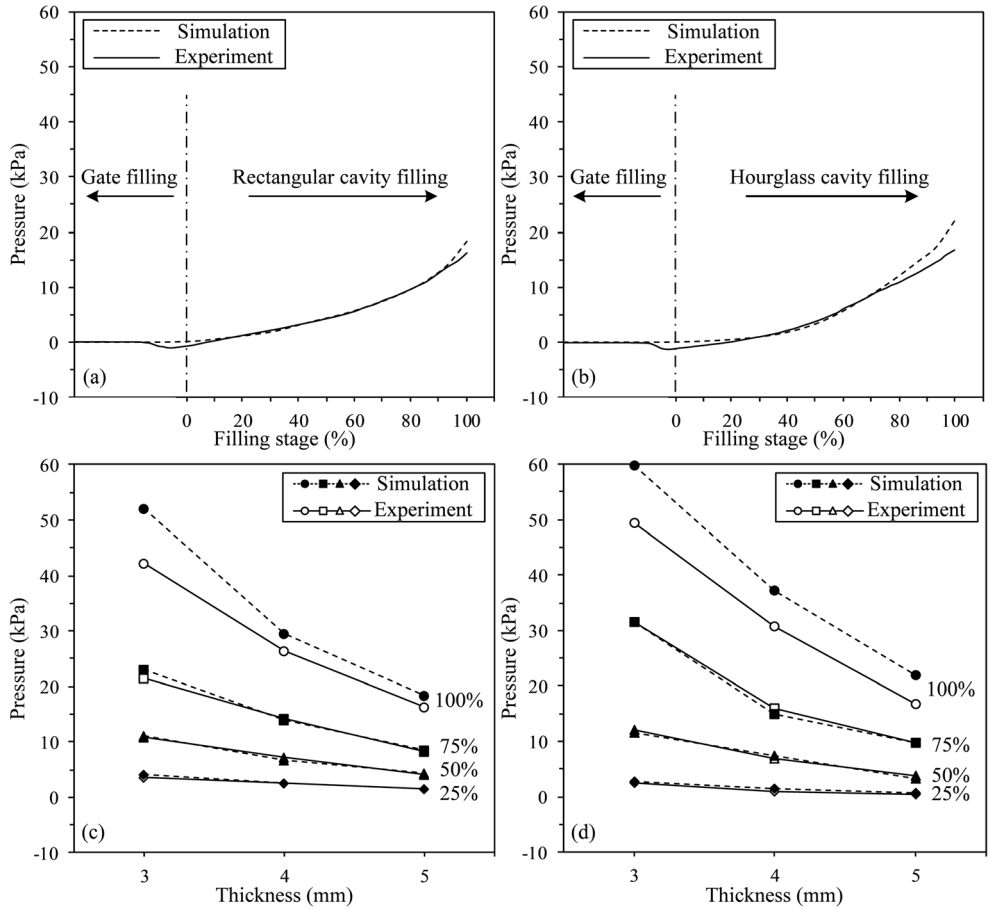

Fig. 8 Typical simulated and experimental pressure profiles obtained at sensor position P1 and mold thickness of 5 mm for (a) rectangular, (b) hourglass cavities, and (c-d) comparison of experimental and simulated pressures at different filling stages and thicknesses (injection temperature = 90 °C)

to bypass the overpressure obtained by numerical simulations and predict the injection pressure, especially at the end of the mold filling. To that end, the four experimental pressure profiles measured at the sensor position P1 for the limit conditions (as illustrated in Fig. 9a-b with white and black dots) were used to obtain fitted coefficients and propose a model for each mold cavity, as denoted by continuous and dashed lines in Fig. 9a-b. For the rectangular and hourglass mold cavities, the pressure profiles can be described by the third-order and sigmoid functions presented in Eq. (9) and Eq. (10) according to the percentage of filling stage (X) and the desired thickness (Y) or temperature (Y), for a constant temperature of 90 °C or constant mold thickness of 4 mm, respectively.

$$P_{rectangular}(X,Y) = a + bX + cY + dX^2 + eXY + fX^3 + gX^2Y \quad (9)$$

$$P_{hourglass}(X,Y) = h + \frac{(i/Y) - h}{j + l\exp(-kX)} \quad (10)$$

These two models and their related coefficients reported in Table 4 were obtained using the Curve Fitting Toolbox implemented in MATLAB ($R^2 > 99.8\%$). To simplify the model, the negative pressures observed experimentally at the beginning of the filling stage (see Fig. 7 & Fig. 8) were removed and considered to be zero. These models were then used to predict the pressure profiles for an injection temperature of 90 °C and a mold thickness of 4 mm (Fig. 9c). The experimental data were then used to validate the predicted pressure profiles calculated by phenomenological models. As seen in Fig. 9c, this approach can be used to better assess the pressure at the end of the mold filling, with a maximum relative difference of about 20% instead of 33.1%, as previously predicted by numerical simulations.

Conclusion

The potential to simulate the mold filling behavior of metallic-based feedstock with the low-pressure powder injection molding process (LPIM) using the commercial software Autodesk Moldflow Synergy 2019 was investigated. A feedstock formulated from 17 to 4 PH stainless steel powder and a wax-based binder system (solid loading of 60 vol.%) was characterized to obtain the melting point, density, thermal conductivity, viscosity, and specific heat capacity. These were then implemented in the numerical model. The simulated injected

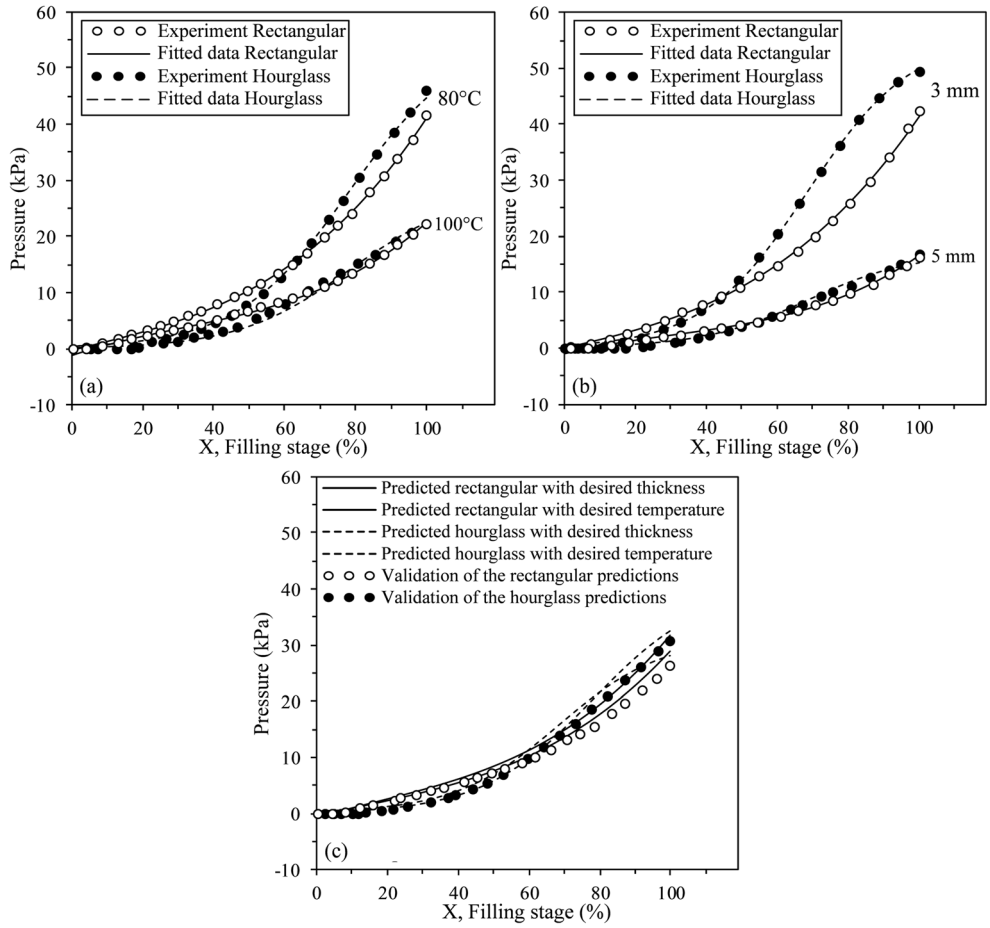

Fig. 9 (a-b) Experimental pressure profiles with superimposed third-order and sigmoid models, and (c) predicted pressure profiles at injection temperature of 90 °C and mold thickness of 4 mm, with corresponding experimental validation.

length, melt front velocity, and injection pressure were validated with real-scale injections in two different mold cavities (rectangular and hourglass) using three thicknesses (3, 4, and 5 mm) and three feedstock temperatures (80, 90, and 100 °C). Note that the impact of binder constituents on debound and sintered properties (shape, bonding, microstructure characteristics, density, etc.) has not been studied in the present work. The present study allowed us to reach some conclusions, which are summarized as follows:

Table 4 Fitting coefficients for the rectangular and hourglass mold cavities

Fitted Coefficient	Y value	
	Temperature	**Thickness**
a	2.819	1.295
b	−5.069 E-2	1.323 E-1
c	−3.929 E-2	−4.604 E-1
d	8.903 E-3	4.044 E-3
e	2.61 E-3	4.332 E-3
f	2.856 E-5	2.404 E-5
g	−1.15 E-4	−1.248 E-3
h	9.289 E-4	3.712 E-4
i	1.245 E-1	2.617 E-3
j	1.123 E-5	8.975 E-5
k	6.363 E-2	6.817 E-2
l	1.622 E-3	9.577 E-4

- Since the experimental and simulated injections were performed at constant volumetric flow, the injected length, as well as the melt front velocity were not influenced by the feedstock temperature, but only by the shape of the mold cavity. In this respect, the injected length and the melt front velocity predicted by the numerical model were in good agreement with the experimental observations, with a maximum relative difference of 0.5% and 3.7%, respectively.
- The simulated pressure profiles were in good agreement with experiments over the majority of the mold filling range, with a relative difference less than 8.3%, but tended to diverge from those measured with sensors at the end of the mold filling. This overestimation observed in the simulated pressure was attributed to an end effect (i.e., absence of mold venting in Moldflow PIM package) that was observed irrespective of the mold shape, feedstock

temperature, sensor location, or mold thickness. Since simulating the pressure values over the whole injection stage is essential, this difference in pressure observed at the end of the mold filling needs to be investigated in future work.

- The decrease in injection pressure with an increase in the melt temperature or an increase in cross-section mold cavity were almost perfectly captured by the numerical model for filling stages lower than 75%.
- The interesting simulation capability of the LPIM injection pressure was, to the best of the authors' knowledge, validated experimentally for the first time, in this study.

Acknowledgments Special thanks to Mr. Sarthak Kapoor for his cooperation and help with the experiments in this research.

Compliance with ethical standards

This work was carried out with the financial support of the Mitacs Globalink Graduate Fellowship and the Natural Science and Engineering Research Council (NSERC, Grant RGPIN-2018-04407).

Conflict of interest The authors declare that they have no conflict of interest.

References

1. Heaney D (2012) Handbook of metal injection molding. Woodhead Publishing
2. German RM, Bose A (1997) Injection molding of metals and ceramics. Metal Powder Industries Federation, Princeton
3. Rei M, Milke E, Gomes R, Schaeffer L, Souza J (2002) Low-pressure injection molding processing of a 316-L stainless steel feedstock. Mater Lett 52(4–5):360–365
4. Costa C, Michels A, Kipper M (2018) Welding lines formation in holes obtained by low pressure injection molding of ceramic parts. Cerâmica 64(369):97–103
5. Medvedovski E, Peltsman M (2013) Low pressure injection molding of advanced ceramic components with complex shapes for mass production. Advanced Processing and Manufacturing Technologies for Structural and Multifunctional Materials VI- 36th International Conference on Advanced Ceramics and Composites, ICACC 2012, January 22–27, 2012, American Ceramic Society, Daytona Beach, FL, United states:35–51
6. Mangels JA (1994) Low-pressure injection molding. Am Ceram Soc Bull 73:37–41
7. Zorzi JE, Perottoni CA, Da Jornada JAH (2003) Wax-based binder for low-pressure injection molding and the robust production of ceramic parts. Ind Ceram 23:47–49
8. Hidalgo J, Abajo C, Jimenez-Morales A, Torralba JM (2013) Effect of a binder system on the low-pressure powder injection moulding of water-soluble zircon feedstocks. J Eur Ceram Soc 33(15-16): 3185–3194
9. Hausnerova B, Kasparkova V, Hnatkova E (2016) Rheological and thermal performance of newly developed binder Systems for Ceramic Injection Molding, VIII international conference on "times of polymers and composites": from aerospace to nanotechnology. American Institute of Physics, USA: 020120–020124
10. Goncalves AC (2001) Metallic powder injection molding using low pressure. J Mater Process Technol 118(1-3):193–198
11. Julien B, Després M (2006) Metal injection Moulding: a near net shape fabrication method for the manufacture of turbine engine component, cost effective manufacture via net shape processing, research and technology organisation (NATO). Amsterdam, Netherlands: 8.1–8.16
12. Nor NHM, Muhamad N, Jamaludin KR, Ahmad S, Ibrahim MHI (2011) Characterisation of titanium alloy feedstock for metal injection Moulding using palm stearin binder system. Adv Mater Res 264-265(1):586–591
13. Aslam M, Ahmad F, Yusoff P S M B M, Altaf K, Omar M A, Abdul Khalil H P S (2016) Raza M.R., Investigation of Rheological Behavior of Low Pressure Injection Molded Stainless Steel Feedstocks. Adv Mater Sci Eng 2016
14. Fareh F, Demers V, Demarquette NR, Turenne S, Scalzo O (2017) Influence of segregation on rheological properties of wax-based feedstocks. Powder Technol 320:273–284
15. Zhang Y, Basso A, Christensen SE, Pedersen DB, Staal L, Valler P, Hansen HN (2020) Characterization of near-zero pressure powder injection moulding with sacrificial mould by using fingerprint geometries. CIRP Ann 69(1):185–188
16. Thornagel M (2010) Simulating flow can help avoid mould mistakes. Met Powder Rep 65(3):26–29
17. Ilinca F, Hétu JF, Derdouri A, Stevenson J (2002) Metal injection molding: 3D modeling of nonisothermal filling. Polym Eng Sci 42(4):760–770
18. Ilinca F, Hetu J-F, Derdouri A, Stevenson J (2002) Three-dimensional filling and post-filling simulation of metal injection molding. J Inject Molding Technol 6(4):229
19. Ahn S, Chung S, Atre S, Park S, German R (2008) Integrated filling, packing and cooling CAE analysis of powder injection moulding parts. Powder Metall 51(4):318–326
20. Tseng H-C, Chang Y-J, Tien C-H, Hsu C-H (2014) Prediction of powder concentration for filling simulation of metal injection molding. In: SPE Annual Tech meeting
21. Zheng Z-X, Wei X, Zhou Z-Y, Zhu Q-L (2008) Numerical simulation of tungsten alloy in powder injection molding process. Trans Nonferrous Met Soc 18(5):1209–1215
22. Bilovol V, Kowalski L, Duszczyk J, Katgerman L (2003) Comparison of numerical codes for simulation of powder injection moulding. Powder Metall 46(1):55–60
23. Bilovol V, Kowalski L, Duszczyk J, Katgerman L (2006) The effect of constitutive description of PIM feedstock viscosity in numerical analysis of the powder injection moulding process. J Mater Process Technol 178(1–3):194–199
24. Sardarian M, Mirzaee O, Habibolahzadeh A (2017) Influence of injection temperature and pressure on the properties of alumina parts fabricated by low pressure injection molding (LPIM). Ceram Int 43(6):4785–4793
25. Sardarian M, Mirzaee O, Habibolahzadeh A (2017) Mold filling simulation of low pressure injection molding (LPIM) of alumina: effect of temperature and pressure. Ceram Int 43(1):28–34
26. Sardarian M, Mirzaee O, Habibolahzadeh A (2017) Numerical simulation and experimental investigation on jetting phenomenon in low pressure injection molding (LPIM) of alumina. J Mater Process Technol 243:374–380
27. Ben Trad MA, Demers V, Côté R, Sardarian M, Dufresne L (2020) Numerical simulation and experimental investigation of mold filling and segregation in low-pressure powder injection molding of metallic feedstock. Adv Powder Technol 31(3):1349–1358
28. Zhang MM, Lin B Simulation of ceramic injection molding for zirconia optical ferrule. Key Eng Mater 336–338:997–1000
29. Jiang B-Y, Wang L, Xie L, Huang B-Y (2005) Viscosity model parameters fitting of feedstock in MIM simulation and analysis. Chin J Nonferrous Met 15(3):429–434

30. Binet C, Heaney D, Spina R, Tricarico L (2005) Experimental and numerical analysis of metal injection molded products. J Mater Process Technol 164:1160–1166
31. Koszkul J, Nabialek J (2004) Viscosity models in simulation of the filling stage of the injection molding process. J Mater Process Technol 157(158):183–187
32. Wang W, Li X, Han X (2012) Numerical simulation and experimental verification of the filling stage in injection molding. Polym Eng Sci 52(1):42–51
33. Leverkoehne M, Coronel-Hernandez J, Dirscherl R, Gorlov I, Janssen R, Claussen N (2001) Novel binder system based on paraffin-wax for low-pressure injection molding of metal-ceramic powder mixtures. Adv Eng Mater 3(12):995
34. Majewska-Glabus I, Zhuang L, Vetter R, Duszczyk J (1995) Thermal debinding of Fe 3 Al-X metal powder compacts. J Mater Sci 30(24):6209–6217
35. Y-m L, Liu X-Q, Luo F-h, Yue J-L (2007) Effects of surfactant on properties of MIM feedstock. Trans Nonferrous Met Soc 17(1):1–8
36. ASTM-B923–16 (2016) Standard test method for metal powder skeletal density by helium or nitrogen Pycnometry. ASTM International, West Conshohocken, PA
37. ASTM-D3418–15 (2015) Standard test method for transition temperatures and enthalpies of fusion and crystallization of polymers by differential scanning Calorimetry. ASTM International, West Conshohocken, PA
38. ASTM-E1269–11 (2018) Standard test method for determining specific heat capacity by differential scanning Calorimetry. ASTM International. West Conshohocken, PA
39. Borup KA, de Boor J, Wang H, Drymiotis F, Gascoin F, Shi X, Chen L, Fedorov MI, Müller E, Iversen BB, Snyder GJ (2015) Measuring thermoelectric transport properties of materials. Energy Environ Sci 8(2):423–435
40. Xie P, Guo F, Jiao Z, Ding Y, Yang W (2014) Effect of gate size on the melt filling behavior and residual stress of injection molded parts. Mater Des 53:366–372
41. Bosioc A, Susan-Resiga R, Muntean S (2008) Design and manufacturing of a convergent-divergent test section for swirling flow apparatus. In: proceedings of the 4th German–Romanian workshop on Turbomachinery hydrodynamics (GRoWTH)

Publisher's note Springer Nature remains neutral with regard to jurisdictional claims in published maps and institutional affiliations.